CFD Simulations of Hydrodynamic/Thermal Coupling Phenomena in a Bubble Column with Internals

Cédric Laborde-Boutet and Faiçal Larachi
Dept. of Chemical Engineering, Laval University, Québec, Canada G1V 0A6

Nicolas Dromard and Olivier Delsart
TOTAL—Research Center of Gonfreville, Refining & Process, Harfleur F-76700, France

Pierre-Emmanuel Béliard
Greth-Leth, CEA-LITEN, rue des Martyrs, Grenoble 38000, France

Daniel Schweich
LGPC—CNRS, ESCPE, Villeurbanne 69616, France

DOI 10.1002/aic.12171

CFD simulations have been carried out in a full three-dimensional, unsteady, Eulerian framework to simulate hydrodynamic/thermal coupling in a bubble column with internals. A first part of the study, dedicated to the hydrodynamic/thermal coupling in liquid single-phase flows, showed that assuming constant wall temperature on the internals constitutes a reasonable approximation in lieu of comprehensive simulations encompassing shell flow and coolant flow together. A second part dealing with the hydrodynamics of gas–liquid flows in a bubble column with internals showed that a RNG k–ε turbulence model formulation accounting for gas-induced turbulence was a relevant choice. The last part used these conclusions to build a hydrodynamic/thermal coupling model of a gas–liquid flow in a bubble column with internals. With a per-phase RNG k–ε turbulence model and assuming constant wall temperature, it was possible to simulate heat transfer phenomena consistent with experimentally measured heat transfer coefficients. © 2010 American Institute of Chemical Engineers *AIChE J,* 56: 2397–2411, 2010

Keywords: bubble column, dynamic simulation, hydrodynamics, multiphase flow, heat transfer

Introduction

Bubble column reactors find myriad applications in biochemical, petrochemical, petroleum, and metallurgical industrial processes.[1–3] These reactors accommodate multiphase flows (gas–liquid or gas-slurry) where the rising gas phase generates a buoyancy-driven flow inducing the recirculation of the liquid (or slurry) phase. This functioning provides good heat and mass transfer characteristics to smooth out temperature and concentration gradients, easy process control and operation, while enabling high throughputs and capacity.[2] This is why a large number of industrial bubble columns are particularly used in highly exothermic processes, such as Fischer-Tropsch synthesis. In these situations, heat transfer

---

Correspondence concerning this article should be addressed to F. Larachi at faical.larachi@gch.ulaval.ca.

efficiency is a key element in the overall reactor performance. One prevailing configuration that industry makes use of consists in arrays of heat exchange tubes immersed inside the bubble column vessel. Local heat exchange is highly depending on hydrodynamics,[4] namely being significantly enhanced by local turbulence.[5] Accordingly, literature reports of empirical studies on heat transfer phenomena in bubble columns have pointed out improved wall-across heat exchange at higher gas superficial velocities[4–10] and worsened heat exchanges at higher liquid viscosities.[5,8,11] Current industrial interest is mostly in churn-turbulent flow operation ($v_g > 0.1$ m s^{-1}, $\alpha_g \geq 0.3$) because it procures higher throughputs,[3] in addition to the higher levels of turbulence which also facilitate heat exchange.[10] However, the hydrodynamic patterns in churn-turbulent flow of bubble columns can be complicated by the presence of heat-exchange internals creating issues when modeling or scaling-up such internal-containing configuration.[4]

Industrial design of bubble column reactors has been mostly based on empirical correlations so far, yet such approaches do not provide much insight into the hydrodynamic patterns[12,13] which condition heat transfer and resulting reactor performance. Computational fluid dynamics (CFD) constitute a promising tool for improving our knowledge of such phenomena, since it allows one to solve mass, momentum, and energy equations locally to obtain detailed depictions of the flow.[14] This technique has considerably grown in importance and interest in the past decade following tremendous developments of computing resources.[15] Nevertheless, the path of CFD modeling and simulations of bubble columns is paved with a number of pitfalls.

CFD simulations of bubble column churn-turbulent flows are still very demanding in terms of computational power, as they have to be carried out in an unsteady[16] full 3D setup[17] to account for the cacophony of the high-frequency three-dimensional instabilities which relentlessly appear, evolve, and die. Consequently, the best trade-off between computational requirements and accuracy is nowadays constituted by Eulerian multi-fluid models. However, constitutive formulations needed for system's closure of the corresponding Reynolds-Averaged Navier-Stokes (RANS) equations raise three significant issues[18]: turbulence modeling, definition of interfacial forces, and determination of local bubble sizes.

Turbulence terms in RANS equations are retrieved from transport equations of the turbulent kinetic energy, k, and the turbulent energy dissipation rate, ε. Such an approach considers isotropic turbulence, which constitutes a simplifying assumption given that turbulence in bubble column flows is known to be anisotropic.[18] Recent studies have nonetheless suggested that k–ε models could reasonably approximate the performance of Reynolds Stress Model simulations[19] or Large Eddy Simulations.[20] Up to now, the most widely used turbulence model in CFD simulation of bubble column flows is the standard k–ε formulation where gas-phase turbulence is neglected.[12,21–26] However, there is currently little justification as for choosing the standard k–ε formulation instead of another, such as renormalization group (RNG) or realizable formulations. Additionally, gas-phase turbulence might not be negligible in highly churn-turbulent flows, where gas holdups in excess of 50% can occur locally.

Interfacial force terms in RANS equations are born from the relative motion of one phase with respect to the other. Inter-phase interactions can be taken as the sum of steady drag, added mass, lift, and turbulent dispersion forces.[18] Among these contributions, drag force is usually considered as being prevalent over other forces.[14,27]

Implementation of bubble population balance is thought to have a significant potential for improving CFD modeling of bubble column flows.[18,26,28–33] Applying constitutive laws for bubble coalescence and break-up[34–38] can indeed allow one to obtain the local mean size of bubbles, thus refining the estimation of turbulence and interfacial force terms. However, the standard k–ε model is known to underestimate the local turbulent energy dissipation rate, ε,[14,18] which leads to a substantial underestimation of bubble break-up rates. As a result, an unrealistic imbalance between simulated coalescence and break-up rates are forecast. Reasonable bubble sizes have been computed only after resorting to artificial tweaks on the break-up rates: inflating local turbulent energy dissipation rate by 10-fold increase,[29–31] or use of a break-up kernel with a higher collision diameter than the collision diameter of the used coalescence kernel.[32] In these cases, prediction capabilities of CFD simulations are sacrificed. Overall, bubble population balance approaches still show some promise, but current implementation does not appear satisfactory.

The determination of local heat transfer characteristics follows the estimation of local hydrodynamic phenomena: velocity wall gradient, laminar sub-layer thickness, turbulent kinetic energy, and turbulent energy dissipation rate. Consequently, the accuracy in the description of heat transfer will directly depend on the relevance of the hydrodynamic model.[39]

In addition to the aforementioned issues in modeling bubble column hydrodynamic and heat transfer, our case of interest is further complicated by the presence of internal cooling tubes, whose influence on the hydrodynamic patterns has not been clearly outlined in the literature.[40] In comparison with the case of a hollow bubble column, the internal tubes would have a significant impact on local turbulence by bounding eddy length-scale.[40] Furthermore, flow structures can be significantly modified, featuring persistent tangential effects. With a non-uniform arrangement of internal tubes, liquid recirculation loops could even be completely redistributed in a complex manner.[40]

This article deals with a study on CFD simulation of hydrodynamic/thermal coupling phenomena of bubble columns in a Eulerian framework, in the specific case of a column featuring a bundle of internal tubes. This work can be divided into three consecutive stages. At first, the relevance of CFD simulations of hydrodynamic/thermal coupling is examined in the case of single-phase flow, which exhibits much simpler hydrodynamics. The second stage consists in defining an appropriate hydrodynamic model for gas–liquid flows in this setup. Ultimately, the selected methods from the first two stages are combined to provide a model for hydrodynamic/thermal coupling phenomena in gas–liquid flow in this bubble column featuring internal tubes.

Description of the Simulated Cases

Set-up description

The simulated setup is based on an experimental bubble column where temperature and heat transfer data have been

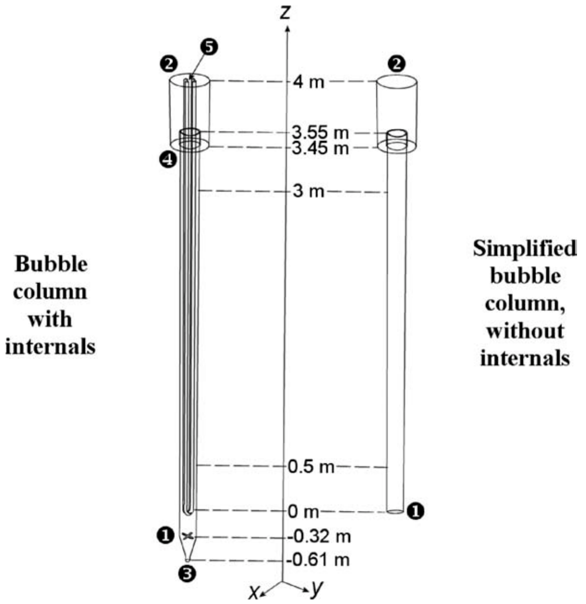

Figure 1. Simulated bubble columns.

1, Gas inlet; 2, Gas outlet; 3, Liquid inlet; 4, Liquid outlet; 5, Coolant flow.

measured.[41] The column has a diameter of 15.1 cm and is equipped with a bundle of two U-shaped cooling tubes, each of them being 2.67 cm in diameter. The total column layout heightens to 4.61 m. Gas is injected in a cross-shaped distributor, while the liquid inlet duct has a diameter of 4.65 cm. The disengagement zone is 30 cm in diameter. Further details of the simulated bubble column are given in Figure 1.

In all simulations with this setup, the column is continuously operated with a liquid superficial velocity of 0.114 m s^{-1}, with respect to the free-passing cross-section of the column comprising the internal tubes (Figure 2). Gas inlet and outlets are shutdown in liquid single-phase simulations. In gas–liquid simulations, the continuous gas flow has a superficial velocity of 0.343 m s^{-1}, with respect to the free-passing cross-section of the column represented in Figure 2.

To outline the impact of the internal tubes on the hydrodynamics, a simplified version of this setup has also been modeled. This simplified model is a 15.1 cm diameter column without internal tubes, whose details are reported in Figure 1. Hydrodynamic gas–liquid simulations were carried out on this setup in batch liquid conditions, and continuous gas flow at $v_g = 0.343$ m s^{-1}.

In these systems, air constitutes the gas phase while the simulated liquid phase corresponds to Syltherm XLT.[42] Simulations accounting for the coolant flow within the internal tubes are carried out with water as the process fluid flowing at a superficial velocity of 0.3 m s^{-1}.

Our simulations are based on an unsteady, full 3D model elaborated with the aid of FLUENT commercial code. Parallel processing on Core-2-Duo CPU has been used to perform the simulations, usually associating 8–10 processors.

Numerical considerations

Numerical Methods. Simulations have been performed with the 3D pressure-based solver in a second order implicit unsteady formulation, available in FLUENT. Gradients are estimated by the Green-Gauss cell based method.

Pressure–velocity coupling was made with the SIMPLE algorithm. As importantly outlined in the literature,[18,21] simulations were carried out with a Third-order Monotone Upstream-Centered Schemes for Conservation Laws (MUSCL) numerical scheme. This Total Variation Diminishing type of numerical schemes tends to minimize numerical diffusion.

Convergence was assumed for each time step as all residuals fall below 10^{-3}, and a maximum of 200 iterations per time step was considered if the residuals failed to pass these thresholds.

Grid Resolution. Meshing the aforementioned systems has been performed with the GAMBIT software. For the column with internal tubes, a hybrid type of grid was used with the purpose of obtaining a maximum of hexahedral structured mesh and a minimum of tetrahedral cells, without any tetrahedral cell yielding an excessive skewness factor. Tetrahedral meshing was unavoidable around the cross-shaped gas distributor and around the U-shaped bottom end of the internal cooling tubes that are positioned at right angle. Structured hexahedral meshing was achieved for the rest of the column, including the necessary wall-refinements for better depiction of velocity and temperature gradients, as shown in Figure 2.

Typical cell size within the column bulk has been defined along $\Delta x = \Delta y = 8$ mm, and $\Delta z = 20$ mm. The ''wall-refinement'' consists of several rows of thinner cells in the vicinity of the wall (three rows for the outer wall, two rows for each tube wall), ranging from 2 mm thick (attached to the wall) to 3 mm thick (towards the bulk region), keeping Δz identical to the bulk cells. As the inside of the tubes is not meshed, this system has 179,248 cells. Meshing the coolant side of the tubes yields 59,566 additional cells (total number of cells: 238,814).

Structured hexahedral meshing was performed for the column without internal tube, generating 197,040 cells.

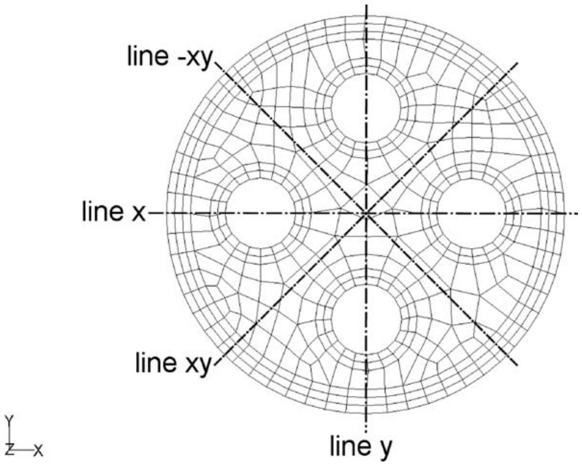

Figure 2. Cross-section of the grid at z = 3 m, featuring hexahedral structured cells and wall-refinements in the column side.

The mesh within the cooling tubes is not shown.

Averaging Times in Liquid Single-Phase Flow Simulations. Given the relationship between hydrodynamics and heat transfer, pseudo-steady-state was assumed after stabilization of the liquid outlet temperature, typically after a time lapse of 200 s. A preventive time lapse of 100 additional seconds is run subsequently to confirm flow and heat transfer stability. Afterwards, the time averaging process was enabled for the next 200 s.

Time steps of 0.1 s would have been sufficient to account for the transient instabilities of the flow given the mean axial velocities ($v_z \approx 0.114$ m s^{-1}) and cell height ($\Delta z = 20$ mm). Use a time step of 0.01 was chosen to facilitate convergence.

Averaging Times in Gas–Liquid Flow Simulations. Flow dynamics have a much shorter time scale in gas–liquid churn-turbulent flow than in the aforementioned liquid single-phase flow simulations. In gas–liquid simulations, a part of the bubble column was defined between $z = 0.5$ m and $z = 3$ m, which supposedly corresponds to the fully-developed region of the flow (Figure 1). Attainment of pseudo-steady-state was assumed after the fluctuations on the overall gas holdup will have stabilized, typically after a time lapse of 60 s. Next, a preventive time lapse of 40 more seconds is run systematically to confirm flow stability. Subsequently, the time averaging process was enabled for the following 60 s.

Convergence concerns constrained us to use a time step no greater than 0.0001 s in these simulations, as well as low values of under-relaxation factors (typically 0.01). The low values of the under-relaxation factors have the effect of extending artificially the time scale of the simulated flow fluctuations. This effect can be compensated by a choice of longer averaging times, but this could not be afforded in practice (the ratio between simulation time and time step size being very high and multiphase-flow yielding a greater number of equations to be solved at each time step). The low values of the under-relaxation factors are taken into consideration when the results are discussed later.

Data post-processing

Profiles. Hydrodynamic data of the simulated flow are mostly presented in the Results and discussion section as radial profiles of time-averaged flow fields that have been axially averaged over the fully developed region of the flow (between $z = 0.5$ m and $z = 3$ m), at four different azimuthal positions. These four tangential positions are noted as "line x," "line y," "line xy," and "line –xy" and reported in Figure 2: two tangential lines (line x and line y) span across the internal tubes while the two others (line xy and line –xy) are at equal distance from the tubes.

Temperature radial profiles are time-averaged values that have been axially averaged at various heights: the "down" part of the tubes corresponds to 0 m $\leq z \leq$ 0.5 m while the "up" section of the tubes corresponds to 3 m $\leq z \leq$ 3.5 m.

Temperature axial profiles are also time-averaged values. The central temperature axial profile is taken at the column centreline. When the coolant flow is simulated, tube temperature axial profiles are retrieved as well, corresponding to time-averaged values at each tube centreline.

Convention for Calculating Heat Transfer Coefficients. Global heat transfer coefficients are calculated from simulation results and compared with the global heat transfer coefficients retrieved from experimental data.

In the simulations, fluid inlet temperatures are uniform across the respective sections. However, fluid outlet temperatures are not. Overall outlet temperatures are taken as mixing-cup temperatures, defined as (Eq. 1).

$$T_{\mathrm{out}} = \frac{1}{Q} \iint_{S_{\mathrm{out}}} v(s)T(s)ds \tag{1}$$

The global heat balance is expressed by (Eq. 2).

$$\dot{Q} = \dot{m}\left(c_{\mathrm{P},T_{\mathrm{out}}} T_{\mathrm{out}} - c_{\mathrm{P},T_{\mathrm{in}}} T_{\mathrm{in}}\right) \tag{2}$$

Experimentally, global heat transfer coefficients are calculated via (Eq. 3).

$$H = \frac{\dot{Q}}{S\,\Delta T_{\mathrm{lm}}}. \tag{3}$$

The mean logarithmic temperature difference that is used in Eq. 3 is calculated by Eq. 4, which assumes an ideal shell-tube heat exchange. No heat exchange is considered at the outer wall of the column.

$$\Delta T_{\mathrm{lm}} = \frac{\left(T_{\mathrm{out}} - T_{\mathrm{tube,Up}}\right) - \left(T_{\mathrm{in}} - T_{\mathrm{tube,Down}}\right)}{\ln\left(\frac{T_{\mathrm{out}} - T_{\mathrm{tube,Up}}}{T_{\mathrm{in}} - T_{\mathrm{tube,Down}}}\right)} \tag{4}$$

For the sake of comparison between experimental and simulated cases, estimation of the global heat transfer coefficient from simulated data is based on the same relations (Eqs. 3 and 4). Experimentally, coolant temperatures are taken as the tube temperatures, so the same will be considered in these calculations when the coolant flow is simulated. When a thermal boundary condition is set at the tube wall (coolant flow not simulated), the tube wall temperature is considered in Eqs. 3 and 4, even in the hypothetical case of isothermal tubes (where $T_{\mathrm{tube,Up}} = T_{\mathrm{tube,Down}}$).

This convention doesn't allow a straightforward comparison of simulated global heat transfer coefficients, between cases where coolant flow is simulated and cases where a thermal boundary condition is defined at the tube wall. In experiments, and when the coolant flow is simulated, the global heat transfer coefficients accounts for the heat transfer resistance in the shell side and in the tube side. When a boundary condition is set at the tube walls (constant heat flux density or constant wall tube temperature), only the shell-side heat transfer resistance is taken into consideration.

Physical models

Liquid Single-Phase Simulations

Fluid properties. Two different cases were considered in liquid single-phase simulations, as far as phase physical properties are concerned. The simplest case assumes that fluid properties (ρ, μ, c_{p}, λ) are set to constants, equal to the fluid properties at 20°C (293.15 K).

The more elaborate case considers fluid properties as dependent on temperature. Density, specific heat capacity, and thermal conductivity are taken as third-order polynomial of temperature whose coefficients are fitted on the manufacturer's data.[42] Viscosity is set as a function of temperature along a power-law formulation fitted on the manufacturer's data.[42]

RANS equations. RANS equations in single phase simulations are given by

$$\frac{\partial \rho}{\partial t} + \mathrm{div}\left(\rho \vec{\mathbf{U}}\right) = 0 \tag{5}$$

$$\frac{\partial\left(\rho \vec{\mathbf{U}}\right)}{\partial t} + \mathrm{div}\left(\rho \vec{\mathbf{U}} \otimes \vec{\mathbf{U}}\right) = -\nabla p + \rho \vec{g} + \mathrm{div}\left(\overset{\Rightarrow}{\mathbf{T}}_i\right) - \mathrm{div}\left(\rho \vec{u'} \otimes \vec{u'}\right) \tag{6}$$

Two settings of RANS equations are tested. The "laminar" setting simply neglects turbulence phenomena, cancelling the Reynolds Stress tensor (i.e., the last term of Eq. 6). The "turbulent" setting accounts for turbulence phenomena, computing the Reynolds Stress tensor via the RNG k–ε model (Eqs. 7–13).

$$\rho\, \overline{\vec{u'} \otimes \vec{u'}} = -\frac{2}{3}\left(\rho\, k + \rho\, \mu_t\, \mathrm{div}\left(\vec{\mathbf{U}}\right)\right)\overset{\Rightarrow}{\mathbf{I}} + \rho\, \mu_t \left(\nabla \vec{\mathbf{U}} + \left(\nabla \vec{\mathbf{U}}\right)^T\right) \tag{7}$$

$$\mu_{\mathrm{t}} = \rho\, C_\mu \frac{k^2}{\varepsilon} \tag{8}$$

$$\frac{\partial(\rho\, k)}{\partial t} + \mathrm{div}\left(\rho\, k\, \vec{\mathbf{U}}\right) = \mathrm{div}\left(\left(\frac{\mu + \mu_{\mathrm{t}}}{\sigma_{\mathrm{k,eff}}}\right)\overrightarrow{\nabla k}\right) + G_{\mathrm{k}} - \rho\, \varepsilon \tag{9}$$

$$\frac{\partial(\rho\, \varepsilon)}{\partial t} + \mathrm{div}\left(\rho\, \varepsilon\, \vec{\mathbf{U}}\right) = \mathrm{div}\left(\left(\frac{\mu + \mu_{\mathrm{t}}}{\sigma_{\varepsilon,\mathrm{eff}}}\right)\overrightarrow{\nabla \varepsilon}\right) + \frac{\varepsilon}{k}\left(C_{1,\varepsilon}\, G_{\mathrm{k}} - C_{2,\varepsilon}\, \rho\, \varepsilon\right) - R_\varepsilon \tag{10}$$

$$G_k = \mu_{\mathrm{t}}\, S^2 \tag{11}$$

$$S = \sqrt{2\, S_{\mathrm{ij}}\, S_{\mathrm{ij}}} \tag{12}$$

$$\overset{\Rightarrow}{\mathbf{S}} = \frac{1}{2}\overset{\Rightarrow}{\varepsilon} = \frac{1}{2}\left(\nabla \vec{\mathbf{U}} + \left(\nabla \vec{\mathbf{U}}\right)^T\right) \tag{13}$$

The $C_{1,\varepsilon}$ and $C_{2,\varepsilon}$ constants of the RNG formulation have values of 1.42 and 1.68, respectively. The effective Schmidt numbers σ_{eff} from Eqs. 9 and 10 are determined by (Eq. 14).

$$\left|\frac{\left(\frac{1}{\sigma_{\mathrm{eff}}}\right) - 1.3929}{\left(\frac{1}{\sigma_0}\right) - 1.3929}\right|^{0.6321} \left|\frac{\left(\frac{1}{\sigma_{\mathrm{eff}}}\right) + 2.3929}{\left(\frac{1}{\sigma_0}\right) + 2.3929}\right|^{0.3679} = \frac{\mu}{\mu + \mu_{\mathrm{t}}} \tag{14}$$

where $1/\sigma_0 \approx 1.0$. An interesting feature of the RNG k–ε models lies in the R_ε term, which corrects the local estimation of the turbulent energy dissipation rate (Eq. 10), via the local strain rate (Eq. 15).

$$R_\varepsilon = \frac{C_\mu\, \rho\, \eta^3 \left(1 - {}^{\eta}\!/_{\eta_0}\right)}{1 + \beta\, \eta^3}\frac{\varepsilon^2}{k} \tag{15}$$

where $\beta = 0.012$, $\eta_0 = 4.38$, while η is defined as (Eq. 16).

$$\eta = S\frac{k}{\varepsilon} = \frac{k}{\varepsilon}\sqrt{\frac{G_{\mathrm{k}}}{\mu_{\mathrm{t}}}} \tag{16}$$

The simulated single-phase flows are moderately turbulent. Comparing the laminar with the turbulent setting is a way to highlight the role of turbulence in heat transfer phenomena.

Energy equation. Heat transfer descriptions are based on the energy transport equation (Eq. 17).

$$\frac{\partial(\rho\, E)}{\partial t} + \mathrm{div}\left((\rho\, E + p)\vec{\mathbf{U}}\right) = \mathrm{div}(\lambda_{\mathrm{eff}} \nabla T) \tag{17}$$

The energy E of the simulated incompressible fluid is given by the sum of its enthalpy and its kinetic energy (Eq. 18).

$$E = h + \frac{\left\|\vec{\mathbf{U}}\right\|^2}{2} \tag{18}$$

The enthalpy h is retrieved from the fluid specific heat capacity (Eq. 19).

$$h = \int_{T_{\mathrm{ref}}}^{T} c_{\mathrm{p}}\, dT \tag{19}$$

Boundary conditions. In single-phase simulations, the Syltherm XLT liquid inlet is taken as a velocity inlet with an axial velocity $v_{\mathrm{l}} = 1.28$ m s^{-1} to yield a liquid superficial velocity of 0.114 m s^{-1} with respect to the section of the column with internal tubes. Syltherm XLT is introduced into the column at 45°C (318.15 K). It leaves the system via an atmospheric pressure outlet. The wall of the bubble column brings a no-slip condition on the liquid velocity ($v_{\mathrm{wall}} = 0$).

Three different possibilities are considered for modeling the cooling heat transfer from the tubes. The most complete approach consists in modeling the coolant flow inside the internal tubes, solving its relative RANS and energy equations. In this case, the internal tube thickness (and heat transfer resistance) is neglected. Coolant inlet is taken as a velocity inlet with a superficial velocity $v_{\mathrm{c}} = 0.3$ m s^{-1}, at 15°C (288.15 K). The coolant leaves the internal tubes via another atmospheric pressure outlet.

A simplifying case is given by assuming a constant heat flux density at the wall of the internal tubes, which is set at -5000 W m^{-2}.

Another simplifying assumption for modeling the cooling heat transfer lies in setting the internal tubes at a constant temperature, equal to 15°C (288.15 K), without modeling the coolant flow. This case would correspond to a set-up with infinite coolant flow-rate.

In all cases, the outer wall of the column is considered adiabatic.

The heat transfer phenomena occurring at the wall of the internal tubes are described in further details in the Appendix below.

Gas–Liquid Simulations

Fluid properties. In gas–liquid simulations, fluid physical properties (ρ, μ, c_p, λ) are set to constants, equal to their values at 20°C (293.15 K). Setting temperature-dependent physical properties in two-phase flow increases convergence problems significantly, and has been eventually discarded.

RANS equations. RANS equations in gas–liquid flows are given by Eqs. 20 and 21.

$$\frac{\partial(\alpha_p\rho_p)}{\partial t}+\mathrm{div}\left(\alpha_p\rho_p\vec{\mathbf{U}}_{\mathbf{p}}\right)=0 \tag{20}$$

$$\begin{aligned}\frac{\partial\left(\alpha_p\rho_p\vec{\mathbf{U}}_p\right)}{\partial t}&+\mathrm{div}\left(\alpha_p\rho_p\vec{\mathbf{U}}_{\mathbf{p}}\otimes\vec{\mathbf{U}}_{\mathbf{p}}\right)\\&=-\alpha_p\nabla p+\alpha_p\rho_p\vec{\mathbf{g}}+\mathrm{div}\left(\alpha_p\overrightarrow{\overrightarrow{\mathrm{T}}}_p\right)\\&\quad-\mathrm{div}\left(\alpha_p\rho_p\vec{u'}_p\otimes\vec{u'}_p\right)+\sum\vec{\mathbf{F}}_{g-1}\end{aligned} \tag{21}$$

In our previous study on the modeling of gas–liquid churn-turbulent flows of bubble columns without internals, we assessed several assumptions relevant to these cases.[43]

As mentioned in the literature,[14,27,40,43] drag force is largely predominant over other gas–liquid interfacial forces, such as added mass, lift, or turbulent dispersion. Thus, only drag for is accounted for in our simulated gas–liquid flows.

The drag force formulation available in FLUENT takes into account the correction for bubble swarms and local fluid volume fractions (Eq. 22):

$$\vec{\mathbf{F}}_{\mathbf{D,g-l}}=\frac{3\,\alpha_g\,\alpha_l}{4}\frac{\rho_l}{d_g}\,C_D\left(\vec{\mathbf{U}}_g-\vec{\mathbf{U}}_l\right)\left|\vec{\mathbf{U}}_g-\vec{\mathbf{U}}_l\right| \tag{22}$$

The drag force coefficient C_D is retrieved from Morsi Alexander correlation (Eq. 23).[44]

$$C_D=a_1+\frac{a_2}{Re_{g-1}}+\frac{a_3}{Re_{g-1}^2} \tag{23}$$

Re_{g-1} in Eq. 23 is the bubble Reynolds number. The coefficients a_1, a_2, and a_3 in Eq. 23 depend on the value of Re_{g-1} as described elsewhere.[44]

As previously discussed,[43] the application of bubble population balance appears premature at this stage. Consequently, single-sized bubbles are considered in these simulations, with a bubble diameter retrieved from Wilkinson's correlation (Eq. 24).[45]

$$d_g=3\,g^{0,44}\,\gamma^{0,34}\,\mu_l{}^{0,22}\,\rho_l{}^{-0,45}\,\rho_g{}^{-0,11}\,v_g{}^{-0,02} \tag{24}$$

In our air-Syltherm XLT cases, Wilkinson's correlation gives a single bubble size of 3.2 mm in diameter.

Finally, our previous investigations lead us to conclude that the RNG formulation of the k–ε model seems the most appropriate when modeling bubble column flows.[43] Two different modalities of the RNG k–ε model are tested in this study: one is referred to as "dispersed + bubble induced turbulence (BIT)" while the other is labeled "per-phase." In the dispersed + BIT modality, the Reynolds stress tensor terms are only taken into account for the liquid momentum equation (no gas phase intrinsic turbulence) corrected for the liquid pseudo-turbulence induced by the bubbles, whereas the Reynolds stress tensor terms are computed for the momentum equation of each phase in the per-phase modality. The relationship between the Reynolds stress tensor terms and the transport equations of the turbulent kinetic energy and the turbulent energy dissipation rate is given by Eqs. 7 and 8. Transport equations of k and ε are defined as:

$$\begin{aligned}\frac{\partial(\alpha_p\,\rho_p\,k_p)}{\partial t}&+\mathrm{div}\left(\alpha_p\,\rho_p\,k_p\,\vec{\mathbf{U}}_p\right)\\&=\mathrm{div}\left(\alpha_p\left(\frac{\mu_p+\mu_{t,p}}{\sigma_{k,\mathrm{eff},p}}\right)\overrightarrow{\nabla k_p}\right)+\alpha_p\left(G_{k,p}-\rho_p\,\varepsilon_p\right)+\prod\nolimits_k\end{aligned} \tag{25}$$

$$\begin{aligned}\frac{\partial(\alpha_p\,\rho_p\,\varepsilon_p)}{\partial t}&+\mathrm{div}\left(\alpha_p\,\rho_p\,\varepsilon_p\,\vec{\mathbf{U}}_p\right)=\mathrm{div}\left(\alpha_p\left(\frac{\mu_p+\mu_{t,p}}{\sigma_{\varepsilon,\mathrm{eff},p}}\right)\overrightarrow{\nabla\varepsilon_p}\right)\\&+\alpha_p\,\frac{\varepsilon_p}{k_p}\left(C_{1,\varepsilon}\,G_{k,p}-C_{2,\varepsilon}\,\rho_p\,\varepsilon_p\right)-\alpha_p\,R_{\varepsilon,p}+C_{3,\varepsilon}\frac{\varepsilon_p}{k_p}\prod\nolimits_k\end{aligned} \tag{26}$$

The $C_{1,\varepsilon}$, $C_{2,\varepsilon,}$ and $C_{3,\varepsilon}$ constants of the RNG formulation have values of 1.42, 1.68, and 1.2, respectively. The effective Schmidt numbers σ_{eff} from Eqs. 25 and 26 are determined by Eq. 14. The term of kinetic energy production $G_{k,p}$ is given by relations 11–13. The term of strain rate correction $R_{\varepsilon,p}$ is defined by the above relations (Eqs. 15 and 16).

The last term in Eqs. 25 and 26, Π_k, constitutes the turbulence that is induced by the other phase. This parameter is defined by (Eq. 27).

$$\prod\nolimits_k=K_{g-l}\left(2\left(\kappa-k_l\frac{\eta_{g-l}}{1+\eta_{g-l}}\right)+\left(\vec{\mathbf{U}}_g-\vec{\mathbf{U}}_l\right)\cdot\vec{\mathbf{u}}_{dr}\right) \tag{27}$$

The coefficient η_{g-l} from Eq. 27 is defined by the ratio of the bubble Lagrangian time scale over the bubble characteristic relaxation time.[46] K_{gl} from Eq. 27 is an interfacial turbulent drag coefficient which is defined similarly to a drag force coefficient (Eq. 28).

$$K_{g-l}=\frac{3}{4d_g}\alpha_g\,\alpha_l\,\rho_l\,C_D\left|\vec{\mathbf{U}}_g-\vec{\mathbf{U}}_l\right| \tag{28}$$

The parameter κ from Eq. 27 is given by Eq. 29 in the dispersed + BIT modality and by Eq. 30 in the per-phase modality.

$$\kappa=k_l\frac{b+\eta_{g-l}-1}{1+\eta_{g-l}} \tag{29}$$

$$\kappa=k_g \tag{30}$$

where b from Eq. 29 is defined using the added-mass coefficient C_V (typical value of 0.5) by Eq. 31.

$$b=(1+C_V)\left(\frac{\rho_g}{\rho_l}+C_V\right)^{-1} \tag{31}$$

The drift velocity used in Eq. 27 is calculated from Eq. 32 in the dispersed + BIT modality, or from Eq. 33 in the per-phase modality.

$$\vec{\mathbf{u}}_{\mathrm{dr}} = -\left(\frac{\Gamma_{\mathrm{t,g-l}}}{\alpha_{\mathrm{g}}\,\sigma_{\mathrm{g-l}}}\overrightarrow{\nabla\alpha_{\mathrm{g}}} - \frac{\Gamma_{\mathrm{t,g-l}}}{\alpha_{\mathrm{l}}\,\sigma_{\mathrm{g-l}}}\overrightarrow{\nabla\alpha_{\mathrm{l}}}\right) \tag{32}$$

$$\vec{\mathbf{u}}_{\mathrm{dr}} = -\left(\frac{\mu_{\mathrm{t,g}}}{\alpha_{\mathrm{g}}\,\sigma_{\mathrm{g}}}\overrightarrow{\nabla\alpha_{\mathrm{g}}} - \frac{\mu_{\mathrm{t,l}}}{\alpha_{\mathrm{l}}\,\sigma_{\mathrm{l}}}\overrightarrow{\nabla\alpha_{\mathrm{l}}}\right) \tag{33}$$

$\lambda_{\mathrm{t,g-l}}$ from Eq. 32 is a turbulent diffusivity and $\sigma_{\mathrm{g-l}}$ is a dispersion Schmidt number, set by default to 0.75.

RTD simulation. To simulate liquid residence time (RTD) of the bubble column in gas–liquid flow, particle tracking in a Lagrangian reference frame has been carried out, as performed elsewhere.[19] The particles have been defined so that they follow the liquid streamlines along the simulated timescales: they are neutrally buoyant and have a diameter of 10^{-6} m. The turbulent dispersion of particles is modeled by a stochastic approach, assuming interaction between particles and isotropic turbulent eddies. The particle trajectory is calculated by (Eq. 34).

$$\frac{d\vec{\mathbf{U}}_{\mathrm{p}}}{dt} = \frac{3\,\rho_{\mathrm{l}}}{4\,\rho_{\mathrm{p}} d_{\mathrm{p}}}\, C_{\mathrm{D}}\left(\vec{\mathbf{u}}_{\mathrm{p}} - \vec{\mathbf{u}}_{\mathrm{l}}\right)\left|\vec{\mathbf{u}}_{\mathrm{p}} - \vec{\mathbf{u}}_{\mathrm{l}}\right| \tag{34}$$

The liquid velocity $\vec{\mathbf{u}}_{\mathrm{l}}$ is given by the sum of the Reynolds-averaged liquid velocity $\vec{\mathbf{U}}_{\mathrm{l}}$ and the fluctuating liquid velocity $\vec{u'}_{\mathrm{l}}$, the latter being defined by Eq. 35 in Cartesian coordinates.

$$\vec{u'}_{\mathrm{l}} = \begin{pmatrix} \zeta\sqrt{\frac{2}{3}k_{\mathrm{l}}} \\ \zeta\sqrt{\frac{2}{3}k_{\mathrm{l}}} \\ \zeta\sqrt{\frac{2}{3}k_{\mathrm{l}}} \end{pmatrix} \tag{35}$$

In Eq. 35, ζ is a normally distributed random number. A new value of ζ is taken for each passing particle/eddy interaction time. The particle/eddy interaction time is given by the minimum between the eddy lifetime, τ_{λ}, and the eddy crossing time, $\tau_{\lambda,\mathrm{cr}}$, defined by Eqs. 36 and 37, respectively.

$$\tau_{\lambda} = -C_{\mathrm{L}}\frac{k_{\mathrm{l}}}{\varepsilon_{\mathrm{l}}}\log(\xi) \tag{36}$$

$$\tau_{\lambda,\mathrm{cr}} = -\tau_{\mathrm{p,rel}}\ln\left(1 - \left(\frac{\tau_{\lambda,\mathrm{t}}}{\tau_{\mathrm{p,rel}}\left|\vec{\mathbf{u}}_{\mathrm{p}} - \vec{\mathbf{u}}_{\mathrm{l}}\right|}\right)\right) \tag{37}$$

C_{L} is a constant set to 0.15 while ξ is a random number between 0 and 1. $\tau_{\mathrm{p,rel}}$ is the particle relaxation time defined as Eq. 38, and $\tau_{\lambda,\mathrm{t}}$ correspond to the eddy time scale (Eq. 39).

$$\tau_{\mathrm{p,rel}} = \frac{4\,\rho_{\mathrm{p}}^2 d_{\mathrm{p}}}{3\,\rho_{\mathrm{l}}^2\, C_{\mathrm{D}}\left|\vec{\mathbf{u}}_{\mathrm{p}} - \vec{\mathbf{u}}_{\mathrm{l}}\right|} \tag{38}$$

$$\tau_{\lambda,\mathrm{t}} = \sqrt{\frac{3}{2}}C_{\mu}\frac{k_{\mathrm{l}}^{3/2}}{\varepsilon_{\mathrm{l}}} \tag{39}$$

After having ensured that pseudo-steady state was reached (see section Averaging Times in Gas–Liquid Flow Simulations), 82 particles are seeded during 10 successive time steps of 0.0001 s each, delivering 820 particles over 0.001 s corresponding to a pulse injection. A greater number of seeded particles may have been preferable for the sake of statistic representations, but it would have been unwieldy in terms of computational memory requirements. Exiting particles are cumulatively counted over time, yielding a residence time distribution of the particles.

Energy equation. In two-phase flows, heat transfer descriptions are based on the enthalpy transport equation for each phase (Eq. 40).

$$\frac{\partial\left(\alpha_{\mathrm{p}}\rho_{\mathrm{p}}\, h_{\mathrm{p}}\right)}{\partial t} + \mathrm{div}\left(\alpha_{\mathrm{p}}\rho_{\mathrm{p}}\, h_{\mathrm{p}}\vec{\mathbf{U}}_{\mathrm{p}}\right) = -\alpha_{\mathrm{p}}\frac{\partial p_{\mathrm{p}}}{\partial t} - \mathrm{div}\left(\vec{\mathbf{q}}_{\mathrm{p}}\right) + \dot{Q}_{\mathrm{g-l}} \tag{40}$$

The enthalpy h_{q} is retrieved as in Eq. 19, $\vec{\mathbf{q}}_{\mathrm{p}}$ constitutes the heat flux, while $\dot{Q}_{\mathrm{g-l}}$ depicts the inter-phase heat transfer.

The inter-phase heat transfer $\dot{Q}_{\mathrm{g-l}}$ depends on the fluids temperature difference and the inter-phase heat exchange coefficient (Eq. 41).

$$\dot{Q}_{\mathrm{g-l}} = H_{\mathrm{g-l}}\left(T_{\mathrm{g}} - T_{\mathrm{l}}\right) \tag{41}$$

The heat exchange coefficient $H_{\mathrm{g-l}}$ is based on the Nüsselt number of bubbles (Eq. 42).

$$H_{\mathrm{g-l}} = \frac{6\,\alpha_{\mathrm{g}}\,\alpha_{\mathrm{l}}\,\lambda_{\mathrm{l}}}{d_{\mathrm{g}}^2} Nu_{\mathrm{g-l}} \tag{42}$$

The bubble Nüsselt number in Eq. 42 is retrieved from the Ranz-Marshall correlation (Eq. 43).

$$Nu_{\mathrm{g-l}} = 2.0 + Re_{\mathrm{g-l}}^{1/2}\, Pr_{\mathrm{l}}^{1/3} \tag{43}$$

The heat transfer phenomena occurring at the wall of the internal tubes, which drive $\vec{\mathbf{q}}_{\mathrm{p}}$, are described in further details in the Appendix below.

Boundary conditions. In gas–liquid simulations of the column with internals, the Syltherm XLT liquid inlet is taken as a velocity inlet with an axial velocity $v_{\mathrm{l}} = 1.28$ m s^{-1} to yield a liquid superficial velocity of 0.114 m s^{-1} with respect to the section of the column with internal tubes. Liquid is in batch conditions for the case of the column without internal tube.

In all gas–liquid simulations, the air inlet is also taken at a velocity inlet at $v_{\mathrm{g}} = 1.28$ m s^{-1}, resulting in a gas superficial velocity of 0.343 m s^{-1} with respect to the section of the column related to the developed region of the flow. Both phases are injected into the column at 45°C (318.15 K). Both phases exit the system via an atmospheric pressure outlet. A no-slip condition on phases (Eq. 44) is imposed on the wall of the bubble column.

$$\begin{cases} \left\|\vec{\mathbf{U}}_{\mathrm{p}}\right\|_{\mathrm{wall}} = 0 \\ \frac{\partial\alpha_{\mathrm{p}}}{\partial r} = 0 \end{cases} \tag{44}$$

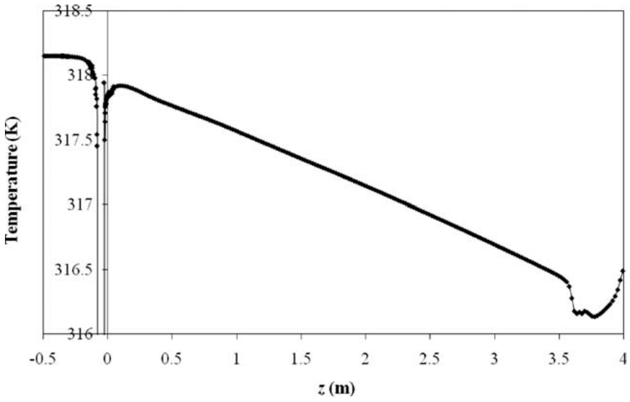

Figure 3. Syltherm XLT temperature at the column centerline, in single-phase simulation with simulated coolant flow and temperature-dependant fluid properties.

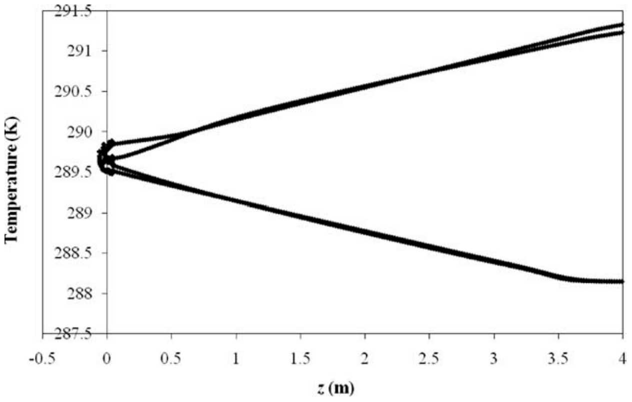

Figure 4. Water temperature at each tube centreline, in single-phase simulation with simulated coolant flow.

The thermal boundary condition for the internal tubes is a constant tube wall temperature, equal to 15°C (288.15 K), without modeling the coolant flow. The outer wall of the column is considered adiabatic.

Results and Discussion

Hydrodynamic/thermal coupling of liquid single-phase flows

Reference Case. A reference case is constituted by a hydrodynamic/thermal coupling model where the flow of Syltherm XLT in the column side and the flow of coolant (water) in the tube side are both simulated. In addition, the simulation is carried out with temperature-dependent fluid properties, to achieve the most realistic representation of an experimental case.

The simulated axial profile of Syltherm XLT temperature at the column centerline is reported in Figure 3, while the axial profiles of coolant temperature at each tube centerline are given in Figure 4.

In Figure 3, the abrupt fall in temperature at $z \approx -0.05$ m corresponds to the region where the U-shaped end of the internal tubes intercepts the column centerline. The Syltherm XLT temperature axial profile is flat before meeting the internal tubes, and then following a linear decrease with increasing column elevation. This linear behavior changes at $z \approx 3.5$ m. This suggests a plug-flow behavior (with axial dispersion) in the column side in the main part of the column, and a sudden hydrodynamic change corresponding to the widening section at the top of the column. Syltherm XLT outlet flow is at an average temperature around 316.6 K, which is subsequent to a global heat exchange $\dot{Q} = 5527.4$ W.

In the coolant side of the tubes, water is injected from the top at 15°C, flows down via two tubes towards (two branches with increasing temperature profiles, Figure 4) the U-shaped section, before flowing upwards (two branches with diminishing temperature profiles, Figure 4) again to the outlet. Figure 4 gives a very relevant temperature evolution of this flow circulation. A flat portion of the coolant temperature axial profile is also noticeable in the upper section ($z \geq 3.6$ m) of the coolest tubes (in down-flow, near the inlet region). It corresponds to the length needed to establish a temperature profile inside the tubes (Figure 5).

As the coolant flows down the tubes, the counter-current heat exchange leads to a water temperature around 289.7 K at the U-shaped section of the tubes. As the coolant flows upwards past the U-shaped section, the co-current heat exchange makes the water exit the system at a mean temperature around 291.3 K. The logarithmic mean temperature difference between the tube side and the column side is $\Delta T_{\mathrm{lm,Down}} = 28.4$ K in counter-current flow, and $\Delta T_{\mathrm{lm,Up}} = 26.8$ K in co-current flow. To define a global heat transfer coefficient, relation (Eq. 3) above is slightly modified into Eq. 45.

$$H = \frac{\dot{Q}}{S_{\mathrm{tubes,Down}}\,\Delta T_{\mathrm{lm,Down}} + S_{\mathrm{tubes,Up}}\,\Delta T_{\mathrm{lm,Up}}} = \frac{2\dot{Q}}{S\left(\Delta T_{\mathrm{lm,Down}} + \Delta T_{\mathrm{lm,Up}}\right)} \tag{45}$$

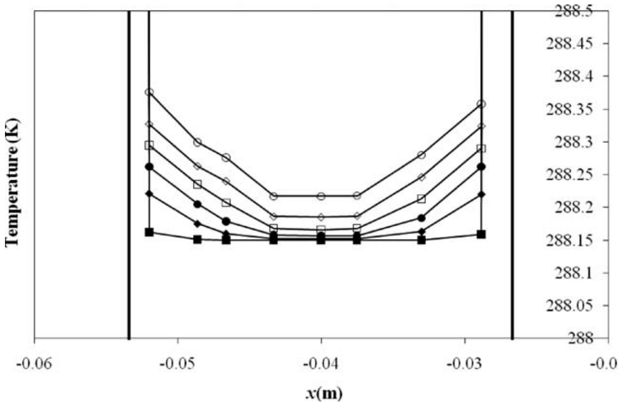

Figure 5. Coolest tube temperature profile at the top of the column along line x, and establishment of the temperature profile within the tube.

T at $z = 4$ m (■), T at $z = 3.9$ m (◆), T at $z = 3.8$ m (●), T at $z = 3.7$ m (□), T at $z = 3.6$ m (◇), T at $z = 3.5$ m (○).

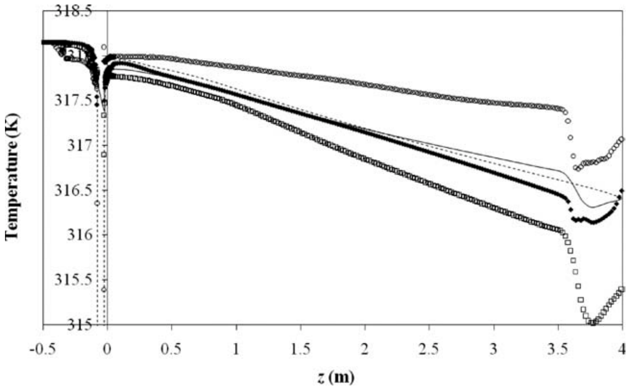

Figure 6. Syltherm XLT temperature at the column centerline in single-phase simulation with constant fluid properties and simulated coolant flow (- - -), constant wall heat flux density (□), constant tube wall temperature (—), and constant tube wall temperature without turbulence terms (○).

Comparison with the reference case (◆).

The global heat transfer coefficient given by Eq. 45 is around 147.1 W m^{-2} K^{-1}. As a reference, the global heat transfer coefficient measured experimentally was 144 W m^{-2} K^{-1}. The extremely close agreement between simulated and experimental data is very satisfying. However, one should realize that the calculation of a global heat transfer coefficient is subject to uncertainties, in both simulated and experimental cases. When calculating the global heat transfer coefficient from simulated data, the result is obtained after accounting for the slight difference in fluid C_P between outlet and inlet. If a single mean C_P value had been used for outlet and inlet conditions alike, the calculated global heat transfer coefficient would have been around 112.6 W m^{-2} K^{-1}.

Constant Fluid Properties. A first simplification of the reference case consists in considering constant fluid properties. To assess the impact of this assumption, a simulation was carried out in the same conditions as the reference case, except for setting constant fluid properties as equal to their respective values at 20°C (293.15 K). The axial profile of Syltherm XLT temperature at the column centerline is shown in Figure 6 (dashed line).

In Figure 6, the temperature axial profile is very close to that of the reference case. As a result, the Syltherm XLT outlet flow is at an average temperature around 316.6 K, which is subsequent to a global heat exchange $\dot{Q} = 4278.1$ W.

The coolant temperature inside the tubes undergoes an evolution that is very similar to the one reported in Figure 4. As the cooling water flows downwards, the counter-current heat exchange heats the water to a temperature around 289.8 K at the tube U-shaped end. Then, the co-current heat exchange causes the water to leave the setup at a mean temperature around 291.5 K. The resulting logarithmic mean temperature difference are $\Delta T_{\mathrm{lm,Down}} = 28.4$ K for the counter-current flow section and $\Delta T_{\mathrm{lm,Up}} = 26.7$ K for the co-current flow section.

The global heat transfer coefficient calculated via Eq. 45 is around 114.1 W m^{-2} K^{-1}. This estimation is lower than the experimental value (144 W m^{-2} K^{-1}), and the estimation given by the reference case (147.1 W m^{-2} K^{-1}). The difference in the energy balance with the reference case doesn't lay much in different estimations of fluid temperature, but rather in the shift of fluid enthalpy that is induced in the reference case.

The greater heat exchange given in the reference case can be explained by a greater turbulence in the vicinity of the tubes. In the reference case, the relationship between viscosity and temperature yields Syltherm XLT viscosity estimations comprised between 0.95 and 1.1 mPa s along the tube walls. In the case of constant fluid properties, Syltherm XLT viscosity is set to 1.4 mPa s. Thus, liquid viscosity is higher in the case of constant fluid properties, which has the effect of dampening turbulence if compared with the reference case (the Reynolds number computed with respect to the hydraulic diameter is around 5400).

Constant Wall Heat Flux. An additional simplifying configuration lies in substituting the coolant flow simulation by the hypothesis of constant wall heat flux. A test was carried out with a constant wall heat flux density of −5000 W m^{-2}. The Syltherm XLT temperature axial profile at the column centerline from this simulation is reported in Figure 6 (hollow squares), where it is compared with the other cases.

The temperature axial profile from the simulation at constant heat flux gives a relatively linear decrease in temperature with increasing column elevation, with lower temperature than in the reference case. This is logical since the overall heat exchange $\dot{Q} = 6729.1$ W, which is higher than in the reference case, has been imposed as a boundary condition.

As a result, the Syltherm XLT temperature at the outlet of the system is around 315.7 K. The constrain of a higher cooling flux has the effect of lowering the wall temperature, so that $T_{\mathrm{tubes,Down}} = 287.5$ K and $T_{\mathrm{tubes,Up}} = 255.7$ K. This results in a ΔT_{lm} value equal to 43.7 K. The corresponding global heat transfer coefficient, calculated by Eq. 3, is equal to 113.1 W m^{-2} K^{-1}.

The global heat transfer coefficient in this case is very similar to the one obtained with simulated coolant flow and constant fluid properties. Fluid properties are temperature-independent in these two cases, so the hydrodynamics in the column side should be similar if not identical. Given the relationships between hydrodynamics and heat transfer, these two cases should exhibit similar heat transfer resistance in the column side. However, the case at constant heat flux density does not account for any heat transfer resistance in the coolant side of the tube. The similarity between the aforementioned cases thus indicates that heat transfer is mainly imposed by the hydrodynamics in the column side of the system.

Nevertheless, realistic wall temperature would only be obtained with prior knowledge of the quantitative heat exchange. Yet, the quantitative heat exchange is generally a sought simulation result rather than a data that is estimated a priori. As shown in this case, the imposed heat flux can yield irrelevant wall temperature, falling below the freezing point of the coolant (water). For these reasons, assuming constant heat flux does not seem a suitable hypothesis of thermal boundary condition in this context.

Constant Wall Temperature. Another simplifying configuration consists in replacing the coolant flow simulation by the assumption of constant wall temperature. This can be experimentally approached with a very high coolant flow-rate which yields experimental results that are even more sensitive to the shell-side heat transfer coefficient. A simulation was run with a constant wall temperature equal to the coolant inlet temperature of the reference case, i.e., 15°C (288.15 K). The resulting axial profile of Syltherm XLT temperature at the column centerline is plotted in Figure 6 (solid line).

In Figure 6, we can observe that the temperature axial profile of the case at constant wall temperature is very close to the case of simulated coolant flow, with constant fluid properties. The Syltherm XLT outlet temperature lies around 316.5 K, corresponding to a heat exchange $\dot{Q} = 4348.3$ W. There is less than 1% difference in global heat exchange between the case at constant wall temperature and the one with simulated coolant flow (with constant fluid properties in both cases). The corresponding ΔT_{lm} value is equal to 29.2 K, which slightly differs from the reference case because $T_{\mathrm{tubes,Up}} = T_{\mathrm{tubes,Down}}$. The resulting global heat transfer coefficient, calculated by Eq. 3, is equal to 109.4 W m^{-2} K^{-1}. This result is similar to the case with simulated coolant flow and constant fluid properties, which confirms that heat transfer is primarily driven by the hydrodynamics in the column side.

Given the similarities in temperature profile and heat transfer coefficients, the assumption of constant tube wall temperature constitutes a good approximation of the case where the coolant flow is simulated.

Constant Wall Temperature, Laminar Flow. A simulation has been carried out at constant wall temperature with the hypothesis of strictly laminar flow. In comparison with the previous case, it is possible to highlight what is the contribution of turbulence phenomena in heat transfer. Thus, wall temperature was set to 15°C (288.15 K) and Reynolds stress terms were not computed. In turns, it affects the energy equation (Eq. 17) since λ_{eff} is normally the sum of the fluid thermal conductivity and the turbulent thermal conductivity (the latter being cancelled in this case). The corresponding axial profile of Sylthem XLT temperature at the column centerline is plotted in Figure 6 (hollow circles), where it is compared with the case including turbulence terms (solid line).

In the laminar case, the temperature decreases more or less linearly with increasing column elevation, until reaching the down-comer region where the change of hydrodynamic pattern changes abruptly. The Syltherm XLT outlet temperature is around 317.2 K in that situation, following a heat exchange $\dot{Q} = 2640.8$ W. Compared with the case of constant wall temperature and inclusion of turbulence, the laminar case yields 60.7% of the heat exchange. As the logarithmic mean temperature difference is equal to 29.5 K (very close to $\Delta T_{\mathrm{lm}} = 29.2$ K in the case including turbulence terms), the global heat transfer coefficient is also reduced to 65.7 W m^{-2} K^{-1}.

This case shows that turbulence has a significant part in heat transfer even at moderately turbulent flow regimes (*Re* $\approx$ 5400). This indicates that the impact of the estimation of turbulent quantities on the simulated heat transfer will be greater in more turbulent flows. The choice of an adequate turbulence model in gas–liquid churn-turbulent flow will have a primary importance for estimating relevant heat transfer phenomena in these cases.

Hydrodynamic of gas–liquid flows in a bubble column with internals

Physical Model Multiphase flow simulations by means of RANS approach require the definition of several closure terms. In the present case, gas–liquid interfacial forces have to be depicted, as well as the turbulent quantities k and ε that define the Reynolds stress. Both of these aspects are also highly influenced by the assumptions made on bubble sizes.

It is generally accepted that drag force is largely predominant over secondary forces such as virtual mass or lift force.[14,27,40] Moreover, our previous study on the hydrodynamics of bubble column flows showed the magnitude of drag force to be more than 100 times that of the other forces.[43] The inclusion of secondary forces (namely the lift force) has also been found to cause numerical instability and convergence problems.[43] Given these aspects, secondary forces have been discarded, leaving drag force as the only gas–liquid interfacial interaction that is accounted for.

For a better depiction of the local contribution of drag force, the computation of the mean local bubble size by means of a bubble population balance would be favorable. However, an inadequacy between the k–ε turbulence models and the break-up kernels transpires from various literature reports[14,18,29–32]: since the turbulent energy dissipation rate is underestimated by k–ε models, it yields underestimated bubble break-up rates and ultimately overestimated bubble sizes. Given this present situation, the description of the local hydrodynamics cannot benefit from the inclusion of bubble population balance calculations. This technique rather lies within future perspectives of this work, as the underestimation of turbulent energy dissipation rate should be addressed first.

In the light of our previous study on the hydrodynamics of bubble column flows,[43] the most appropriate model for our case is based on the RNG k–ε model, accounting for bubble-induced turbulence. The assumption of single sized bubble does not seem to jeopardize the pertinence of the simulated hydrodynamics, despite it being a coarse hypothesis. A significant benefit from choosing the RNG k–ε formulation lies in a more sensible description of turbulent quantities. Mean eddy length scales appear more realistic in this formulation than with the standard or realizable k–ε formulation.[43] A better estimation of the local turbulent quantities should have a substantial impact on the simulated heat transfer.

RTD Simulation. To verify the pertinence of the simulated hydrodynamics, RTD simulation has been carried out in an Euler–Euler–Lagrange framework. In this case, the dispersed + BIT RNG k–ε turbulence model is tested. At pseudo-steady state, a pulse injection of 820 particles is seeded in the liquid inlet. The exiting particles are counted over time, leading to the particle residence time cumulative distribution reported in Figure 7.

The first-order moment of this distribution, μ_1, corresponds to the mean liquid residence time, τ_{l}. In this case, $\mu_1 = 32.8$ s. The liquid space time, calculated from the liquid flow-rates and hold-up, is equal to $\tau_{\mathrm{l}} = 31.7$ s. The first order moment of the RTD is relevant when compared with the established operating conditions.

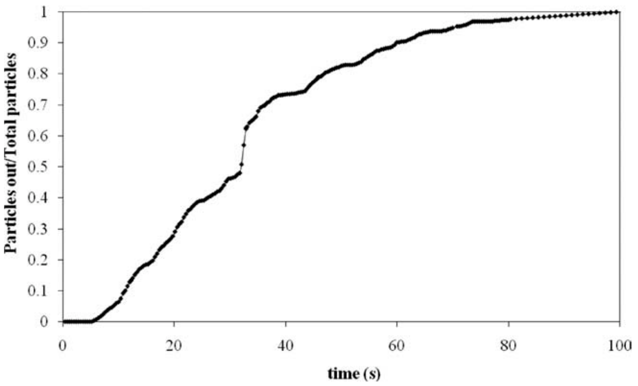

Figure 7. Cumulative distribution of the number of particles exiting the column vs. time.

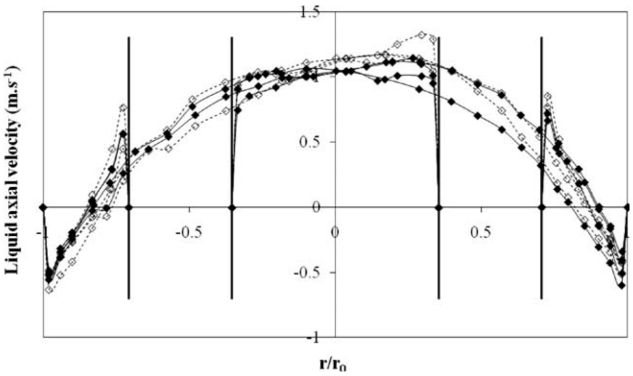

Figure 9. Radial profiles along line x, line y, line xy, and line –xy of the liquid axial velocity in the case of the RNG k–ε model for the dispersed + BIT (- - -) and per-phase (◆) modalities.

The derivative of the cumulative distribution reported in Figure 7 corresponds to the evolution of particle concentration at the liquid outlet over time. It has the same statistic characteristics, as derivation does not affect the distribution moments. This derivative is presented in Figure 8.

In Figure 8, the time at which the highest concentration peak occurs corresponds to the liquid mean residence time. The other noticeable characteristic of this distribution consists in the regular concentration fluctuations that take place periodically, with time cycles of 4–5 s. If the gas space time (in the gas–liquid dispersion) is calculated from its flow-rate and hold-up, we retrieve $\tau_g = 3.7$ s. The period at which particle concentration fluctuates is consistent with the liquid recirculation time, which is comparable with the mean residence time of the gas in the gas–liquid dispersion.

Hydrodynamic Profiles. In a bubble column with internals, the presence of cooling tubes can have a large impact on the hydrodynamics, in a way similar, for instance, to baffles in stirred tanks. The internal tubes restrict the turbulence length scale, or even change circulation patterns.[40] In the present set-up, the simulated hydrodynamics lead to the liquid axial velocity profiles and the gas-holdup profiles reported in Figures 9 and 10, respectively.

As far as liquid circulation is concerned, the overall flow pattern is very similar to the typical liquid recirculation of bubble columns without internal tubes: liquid rises in the center of the column, while it flows down around the outer wall. High gas volume fractions are obtained around the center of the column ($\alpha_g \approx 0.4$), which is consistent with the high gas superficial velocity. The most remarkable simulated feature resulting from the presence of internal tubes consists in the maximum gas hold-up in the vicinity of the internals: α_g can exceed 0.5 on average. These high volume fractions are subsequent to bubble trains (or gas channels) swirling preferentially nearby the internal tubes.

Impact of the Internal Tubes. The influence of the internal tubes can be highlighted by a comparison with the hydrodynamics of a similar bubble column, without internals. Thus, a simulation was carried out on the simplified version of the lacunar setup as described in the Set-up description section, at identical gas superficial velocity (thus, higher volumetric flow-rate due to the different free passing cross-sections of the lacunar vessel vs. the one with internals). The physical model chosen remains the same as far as interfacial forces and bubble size are concerned, while the per-phase modality of the RNG k–ε turbulence model is retained for this case. The resulting liquid axial velocity and gas hold-up profiles are reported in Figures 11 and 12, respectively, where they are compared with the corres-

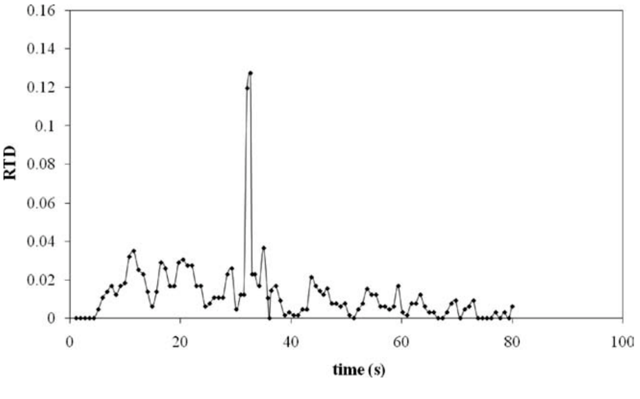

Figure 8. Derivative of the cumulative distribution, yielding the outlet concentration response to a pulse injection.

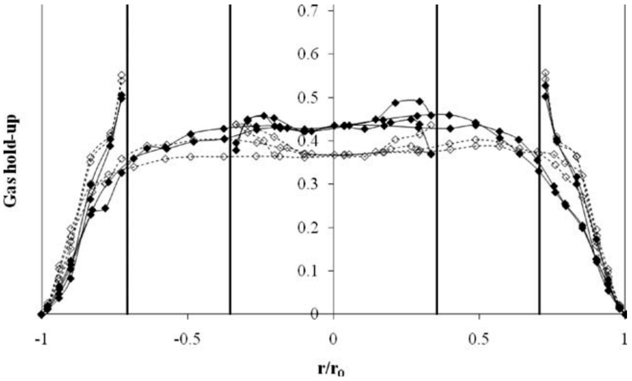

Figure 10. Radial profiles along line x, line y, line xy, and line –xy of the gas hold-up in the case of the RNG k–ε model for the dispersed + BIT (- - -) and per-phase (◆) modalities.

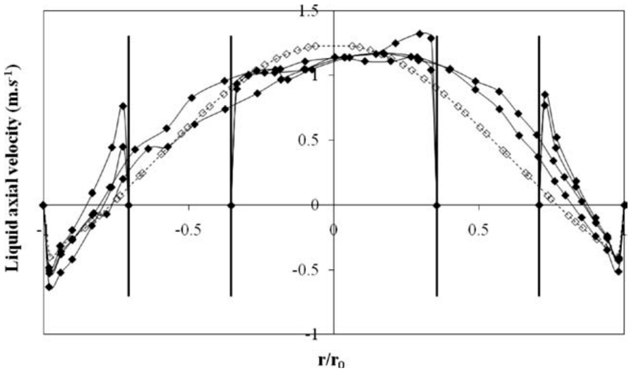

Figure 11. Radial profiles of the liquid axial velocity in the case of the bubble column without internals (- - -), and along line x, line y, line xy, and line –xy in the case of the bubble column with internals (◆).

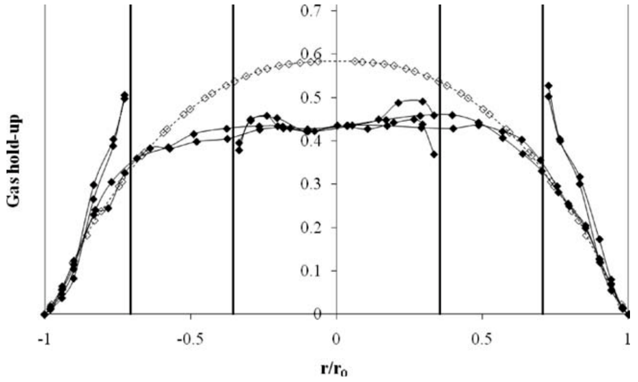

Figure 12. Radial profiles of the gas hold-up in the case of the bubble column without internals (- - -), and along line x, line y, line xy, and line –xy in the case of the bubble column with internals (◆).

ponding profiles that have been obtained with identical physical model on a column with internals.

The radial profiles obtained in the case of the bubble column without internals in Figures 11 and 12 are smoothened as they result from azimuthal averaging. These comparisons highlight the particular gas hold-up distribution in the case of a bubble column with internals: there is a preferential gas flow swirling around the tubes at relatively high velocities. As a result, the gas volume fraction at the column centreline is not as high as what it would be without internals. In addition, at the radial position corresponding to the location of the internals, higher liquid axial velocities are obtained in the case with internals as they follow high velocity gas flows.

However, a more remarkable impact of the internals lies in the change of turbulence length scale. As the relation (Eq. 46) can be used to assess the local eddy length scale, a comparison between the cases with and without internals can be made on a cross-section of the fully-developed region of the flow, as given in Figure 13.

$$\lambda_{\mathrm{l}} = \sqrt{\frac{3}{2}} C_{\mu,l} \frac{k_{\mathrm{l}}^{3/2}}{\varepsilon_{\mathrm{l}}} = \sqrt{\frac{3}{2}} \frac{\mu_{\mathrm{t,l}}}{\rho \sqrt{k_{\mathrm{l}}}} \tag{46}$$

In fact, the flow in the bubble column with internals yields a significantly higher turbulent energy dissipation rate. Eddies are constricted by the tube/tube and tube/outer wall distances. Eventually, the local eddy length scale is noticeably reduced by the presence of internal tubes, being 2–3 times smaller than the eddies in the column without internals. Since heat transfer efficiency is closely related to the local turbulence (see Appendix), the position of internal tubes in a bubble column can have a significant influence on the resulting heat removal.

Hydrodynamic/thermal coupling of gas–liquid flows in a bubble column with internals

The final stage of the study consists in coupling the hydrodynamics of gas–liquid flow in a bubble column with internals with heat transfer. On the basis given in the section

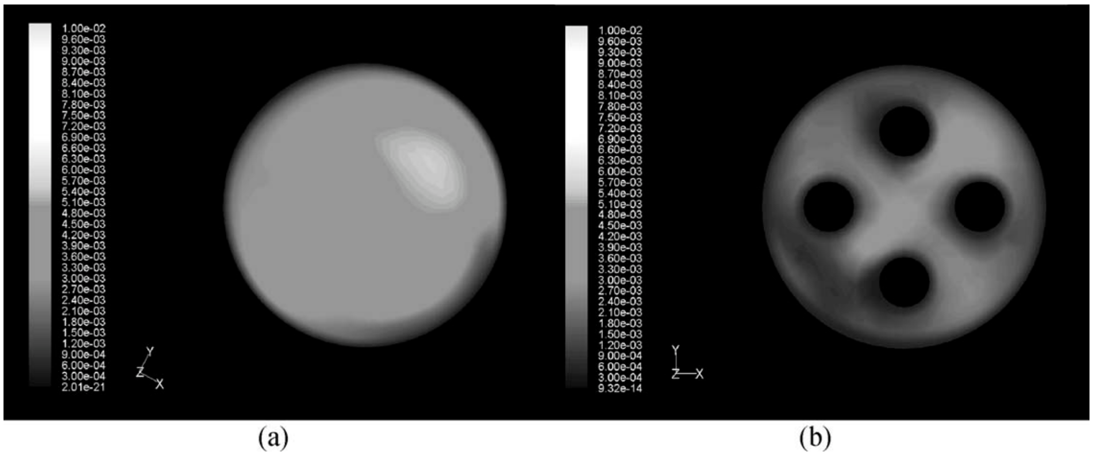

Figure 13. Eddy length scale on a cross-section of the fully-developed region of the flow in the case of the bubble column without internals (a) and with internals (b).

Whiter areas represent high eddy length scales (max ≥ 1 cm) whereas darker areas represent low eddy length scales (min ≈ 0 cm).

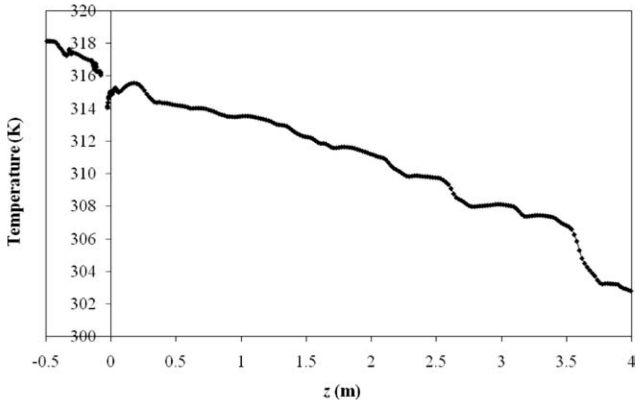

Figure 14. Sylthem XLT temperature at the column centerline, in gas–liquid simulation with constant tube wall temperature.

Hydrodynamic of gas–liquid flows in a bubble column with internals, we can assume the validity of the chosen hydrodynamic model. From our investigations on hydrodynamics/thermal coupling in single-phase flow, we can deduce that the simplifying hypothesis of constant wall temperature is a good approximation of an actual experimental case. Therefore, the hydrodynamic/thermal coupling case in gas–liquid flow combines these two sets of assumptions.

A gas–liquid flow was simulated with the RNG k–ε turbulence model in its per-phase modality, assuming single-sized bubbles (3.2 mm) and accounting only for drag force. Fluid properties were set as constants, to comply with convergence criteria. With a thermal boundary condition of constant internal tube wall temperature (15°C, i.e., 288.15 K), the heat transfer leads to the axial profile of Syltherm XLT temperature at the column centerline reported in Figure 14.

The decrease in temperature with increasing column elevation is much greater in this gas–liquid flow than in single-phase flow, corresponding to a greater heat exchange. This decrease follows minor oscillations along column elevation in Figure 14, which result from the inconvenient choice of low under-relaxation factors. Had the under-relaxation factors and averaging times been greater, we would expect the temperature decrease would have followed a linear trend. The Syltherm XLT outlet temperature is around 303.7 K while the air outlet temperature lies around 303.2 K. This implies that 39248.8 W have been transferred from the liquid phase while 99.0 W have been transferred from the gas phase. This difference is mostly due to the respective mass flow rates of liquid and gas. The calculated ΔT_{lm} value is equal to 21.8 K, yielding a global heat transfer coefficient equal to 1324.1 W m^{-2} K^{-1}.

By comparison with liquid single-phase flow cases, the heat transfer efficiency is much higher in the case of gas–liquid flows. Heat exchange is greater by roughly one order of magnitude, and so is the global heat transfer coefficient. This is due to the much higher levels of turbulence achieved in gas liquid churn-turbulent flows.

The experimental value of the shell-side heat transfer coefficient in the column side in similar experimental conditions is around 1122.7 W m^{-2} K^{-1}.[41] The simulated global heat transfer coefficient compares well with this data. This indicates that the underlying hydrodynamic model and the implementation of heat transfer calculation are carried out satisfactorily.

These heat transfer coefficients suggest that the heat transfer resistance in the column side of the tubes is low, and the heat transfer resistance in the coolant side of the tubes of an actual setup might not be negligible in comparison.

Conclusion

This study on the hydrodynamic/thermal coupling in a bubble column has been carried out through three stages. First, the hydrodynamic/thermal coupling in single-phase flow showed that the boundary condition of constant tube wall temperature constitutes a good approximation of the most realistic case, where the coolant flow is also simulated. The second stage, on the hydrodynamics of gas–liquid bubble column flows, confirmed the relevance of chosen hydrodynamic model: RNG k–ε with bubble-induced turbulence, only drag force accounted for and single sized bubbles. Even though this hydrodynamic model can be improved (with accurate bubble population balance modeling, for instance), it constitutes the best option with the current available resources and knowledge. The last stage consisted of coupling the hydrodynamic model from the second stage with heat transfer calculations, based on the hypothesis of constant tube wall temperature as retained from the first stage. With the much higher levels of turbulence of gas–liquid flows, heat exchange and heat transfer coefficients were greater than in the case of single-phase flow by one order of magnitude. The simulated heat transfer gives a satisfying match with the experimental data, which gives further validation of the underlying gas–liquid hydrodynamic model.

Acknowledgments

C. Laborde-Boutet and F. Larachi acknowledge the financial support from Total. The authors thank Craig Hulet and the LETH team from CEA-LITEN for providing useful data and information, and Éric Lacroix from Total for his supervision.

Notation

Vectors and tensors

$\vec{\mathbf{F}}$ = Force, N
$\vec{\mathbf{g}}$ = Gravity, m s^{-2}
$\dot{\vec{\mathbf{q}}}_{\mathrm{p}}$ = heat flux density, W m^{-2}
$\overrightarrow{\overrightarrow{\mathrm{T}}}$ = Reynolds-averaged viscous stress tensor, Pa
$\overrightarrow{\overrightarrow{\mathbf{S}}}$ = strain rate tensor, Pa
$\vec{\mathbf{U}}$ = Reynolds-averaged velocity, m s^{-1}
$\vec{\mathbf{u}}$ = Velocity, m s^{-1}
$\vec{u'}$ = velocity fluctuation, m s^{-1}
$\overrightarrow{\overrightarrow{\varepsilon}}$ = strain tensor, Pa

Capital letters

A = hydrodynamic parameter
C = coefficient, dimensionless
E = energy, J
G = production of turbulent energy, W m^{-3}
H = global heat transfer coefficient, W m^{-2} K^{-1}
K = turbulent drag coefficient, dimensionless
Nu = Nüsselt number
Pr = Prandtl number
P = Parameter

Q = volumetric flow-rate, m^3 s^{-1}
$\dot{Q}$ = heat exchange, W
R = strain rate correction, W m^{-3} s^{-1}
Re = Reynolds number, dimensionless
T = Temperature, K
S = Area, m^2
S = modulus of the strain rate tensor, s^{-1}

Lowercase letters

a = correlation coefficient, dimensionless
b = virtual mass contribution, dimensionless
d = bubble diameter, m
c_P = specific heat capacity, J kg^{-1} K^{-1}
g = gravity, m s^{-2}
h = enthalpy, J
k = turbulent kinetic energy, m^2 s^{-2}
$\dot{m}$ = mass flow-rate, kg s^{-1}
p = pressure, Pa
r = radius, m
s = surface element, m^2
t = time, s
v = fluid velocity, m s^{-1}
x = Cartesian coordinate, m
y = Cartesian coordinate, m
y^* = dimensionless thermal length
y_T = dimensionless thermal sub-layer thickness
z = Cartesian coordinate, m

Greek letters

α = volume fraction, dimensionless
β = constant
Γ = diffusivity coefficient, m^2 s^{-1}
Δ = difference, any unit
ε = turbulent energy dissipation rate, m^2 s^{-3}
ζ = random number
γ = surface tension, N m^{-1}
η = strain rate coefficient, dimensionless
κ = turbulent energy parameter, m^2 s^{-2}
κ = Von Karman constant
λ = heat conductivity, W m^{-1} K^{-1}
λ = Eddy length scale, m
μ = Viscosity, Pa s
ξ = random number
Π = bubble-induced turbulence term, W m^{-3}
ρ = volumetric mass density, kg m^{-3}
σ = turbulent Schmidt number
τ = Characteristic time, s

Subscripts

0 = reference value
cr = crossing
D = drag
Down = bottom section of the internal tubes
dr = drift
eff = effective
g = gas or gas bubble
in = inlet
i = index
i = cell centroid
j = index
k = turbulent energy
l = liquid
out = outlet
p = phase
p = particle
ref = reference
rel = relative
t = turbulent
tube = internal tube
Up = upper section of the column
V = virtual mass
z = axial
ε = energy dissipation
λ = Eddy
μ = turbulent viscosity

Literature Cited

1. Deckwer WD. *Bubble Column Reactors*. Chichester, UK: John Wiley & Sons, 1992.
2. Dudkovic MP. Trends in catalytic reaction engineering. *Catal Today*. 1999;48:5–15.
3. Dudukovic MP, Larachi F, Mills PL. Multiphase catalytic reactors: a perspective on current knowledge and future trends. *Catal Rev*. 2002;44:123–246.
4. Hulet C, Clément P, Tochon P, Schweich D, Dromard N, Anfray J. Literature review on heat transfer in two- and three-phase bubble columns. *Int J Chem React Eng*. 2009;7:R1.
5. Kantarci N, Borak F, Ulgen KO. Bubble column reactors. *Proc Biochem*. 2005;40:2263–2283.
6. Lewis DA, Field RW, Xavier AM, Edwards D. Heat transfer in bubble columns. *Trans Inst Chem Eng*. 1982;60:40–47.
7. Kim SD, Laurent A. The state of knowledge on heat transfer in three phase fluidized beds. *Int Chem Eng*. 1991;31:284–302.
8. Saxena SC, Chen ZD. Hydrodynamics and heat transfer of baffled and unbaffled slurry bubble columns. *Rev Chem Eng*. 1994;10:195–400.
9. Li H, Prakash A. Heat transfer and hydrodynamics in a three-phase slurry bubble column. *Ind Eng Chem Res*. 1997;36:4688–4694.
10. Lin TJ, Hung-Tzu C. Effects of macroscopic hydrodynamics on heat transfer in a three-phase fluidized bed. *Catal Today*. 2003;79–80:159–167.
11. Quiroz I, Herrera I, Gonzalez-Mendizabal D. Experimental study on convective coefficients in a slurry bubble column. *Int Commun Heat Mass Transfer*. 2003;30:775–786.
12. Ekambara K, Dhotre MT, Joshi JB. CFD simulations of bubble column reactors: 1D, 2D and 3D approach. *Chem Eng Sci*. 2005;60: 6733–6746.
13. Van Baten JM, Ellenberger J, Krishna R. Scale-up strategy for bubble column slurry reactors using CFD simulations. *Catal Today*. 2003;79:259–265.
14. Chen P. Modeling the Fluid Dynamics of Bubble Column Flows. Ph.D. Thesis, St Louis: Sever Insitute of Washington University, 2004.
15. Sanyal J, Marchisio DL, Fox RO, Dhanasekharan K. On the comparison between population balance models for CFD simulation of bubble columns. *Ind Eng Chem Res*. 2005;44:5063–5072.
16. Buwa VV, Ranade VV. Mixing in bubble column reactors: role of unsteady flow structures. *Can J Chem Eng*. 2003;81:402–411.
17. Sokolichin A, Eigenberger G, Lapin A. Simulation of buoyancy driven bubbly flow: established simplifications and open questions. *AICHE J*. 2004;50:24–45.
18. Jakobsen HA, Lindborg H, Dorao CA. Modeling of bubble column reactors: progress and limitations. *Ind Eng Chem Res*. 2005;44: 5107–5151.
19. Le Moullec Y, Potier O, Gentric C, Leclerc JP. Flowfield and residence time distribution simulation of a cross-flow gas–liquid wastewater treatment reactor using CFD. *Chem Eng Sci*. 2008;63:2436–2449.
20. Tabib MV, Roy SA, Joshi JB. CFD simulation of bubble column—an analysis of interphase forces and turbulence models. *Chem Eng J*. 2008;139:589–614.
21. Sokolichin A, Eigenberger G. Applicability of the standard k–ε turbulence model to the dynamic simulation of bubble columns. Part I. Detailed numerical simulations. *Chem Eng Sci*. 1999;54:2273–2284.
22. Pfleger D, Gomes S, Gilbert N, Wagner HG. Hydrodynamic simulations of laboratory scale bubble columns fundamental studies of the Eulerian–Eulerian modelling approach. *Chem Eng Sci*. 1999;54:5091–5099.
23. Padial NT, VanderHeyden WB, Rauenzahn RM, Yarbro SL. Three-dimensional simulation of a three-phase draft-tube bubble column. *Chem Eng Sci*. 2000;55:3261–3273.
24. Van Baten JM, Krishna R. Eulerian simulations for determination of the axial dispersion of liquid and gas phases in bubble columns operating in the churn-turbulent regime. *Chem Eng Sci*. 2001;56:503–512.
25. Pfleger D, Becker S. Modelling and simulation of the dynamic flow behavior in a bubble column. *Chem Eng Sci*. 2001;56:1737–1747.

26. Olmos E, Gentric C, Midoux N. Numerical description of flow regime transitions in bubble column reactors by a multiple gas phase model. *Chem Eng Sci.* 2003;58:2113–2121.
27. Olmos E. Etude Expérimentale et Numérique des Ecoulements Gaz-Liquide en Colonnes à Bulles. Ph. D. Thesis, Nancy, France: Institut National Polytechnique de Lorraine, 2002.
28. Pohorecki R, Moniuk W, Bielski P, Zdrójkowski A. Modelling of the coalescence/redispersion processes in bubble columns. *Chem Eng Sci.* 2001;56:6157–6164.
29. Chen P, Sanyal J, Dudukovic MP. CFD modeling of bubble columns flows: implementation of population balance. *Chem Eng Sci.* 2004;59:5201–5207.
30. Chen P, Sanyal J, Dudukovic MP. Three-dimensional simulation of bubble column flows with bubble coalescence and breakup. *AIChE J.* 2005;51:696–712.
31. Chen P, Sanyal J, Dudukovic MP. Numerical simulation of bubble columns flows: effect of different breakup and coalescence closures. *Chem Eng Sci.* 2005;60:1085–1101.
32. Ekambara K, Nandakumar K, Joshi JB. CFD simulation of bubble column reactor using population balance. *Ind Eng Chem Res.* 2008;47:8505–8516.
33. Homayouni SS, Mehrnia MR, Mostoufi N, Rajabi M, Yazdani A. Bubble size distribution in oil-based bubble columns. *Chem Eng Technol.* 2008;31:1668–1675.
34. Prince MJ, Blanch HW. Bubble coalescence and break-up in air-sparged bubble columns. *AIChE J.* 1990;36:1485–1499.
35. Luo H. Coalescence, Break-Up and Liquid Circulation in Bubble Column Reactors. Ph.D. Thesis, Trondheim, Norway: The Norwegian Institute of Technology, 1993.
36. Luo H, Svendsen HF. Theoretical model for drop and bubble breakup in turbulent dispersions. *AIChE J.* 1996;42:1225–1233.
37. Martínez-Bazán C, Montañéz JL, Lasheras JC. On the breakup of an air bubble injected into a fully developed turbulent flow. Part 1: Breakup frequency. *J Fluid Mech.* 1999;401:157–182.
38. Martínez-Bazán C, Montañéz JL, Lasheras JC. On the breakup of an air bubble injected into a fully developed turbulent flow. Part 2: Size PDF of the resulting daughter bubbles. *J Fluid Mech.* 1999; 401:183–207.
39. Joshi JB. Computational flow modelling and design of bubble column reactors. *Chem Eng Sci.* 2001;56:5893–5933.
40. Larachi F, Desvigne D, Donnat L, Schweich D. Simulating the effects of liquid circulation in bubble columns with internals. *Chem Eng Sci.* 2006;61:4195–4206.
41. Béliard PE, Schweich D, Clément P, Gauthier-Maradei P, Tochon P, Dromard N. *Heat Transfer Metrology Issues in Slurry Bubble Column Reactors.* 8th World Congress of Chemical Engineering: Montreal, Canada: 2009.
42. Dow corning corporation. Syltherm XLT Product Brochure. Available at: http://www.dow.com/heattrans/tech/data.htm.
43. Laborde-Boutet C, Larachi F, Dromard N, Delsart O, Schweich D. CFD simulation of bubble column flows: investigations on turbulence models in RANS approach. *Chem Eng Sci.* 2009;64:4399–4413.
44. Morsi SA, Alexander AJ. An investigation of particle trajectories in two-phase flow systems. *J Fluid Mech.* 1972;55:193–208.
45. Wilkinson PM. Physical Aspects and Scale-up of High Pressure Bubble Columns. D.Sc. Thesis, Groningen, The Netherlands: University of Groningen, 1991.
46. Fluent User's Guide. *Standard, RNG and Realizable k-e models theory— Chapter 12.4*; *Turbulence models*—Chapter 23.5.10. Lebanon: Fluent Inc., 2006.

Appendix

To describe the equations driving wall heat transfer in the FLUENT software, the values allocated to the whole cell next to a wall will be referred to with the *i* index. The length *y* is the distance between the cell centroid and the wall itself.

For a given p-indexed phase, the wall heat transfer equation for a laminar flow is a function of the local temperature gradient ant the thermal conductivity of the phase (Eq. A1).

$$\left\|\vec{\dot{q}}_{\mathrm{p}}\right\| = \lambda_{\mathrm{p}}\left(\frac{\partial T_{\mathrm{p}}}{\partial y}\right)_{y=y_{\mathrm{w}}} = \lambda_{\mathrm{p}}\left(\frac{T_{\mathrm{w}} - T_{\mathrm{p,i}}}{y_{\mathrm{i}}}\right) \tag{A1}$$

The wall heat transfer equation becomes more complex for turbulent flows, as given by Eq. A2.

$$\left\|\vec{\dot{q}}_{\mathrm{p}}\right\| = \frac{\left(T_{\mathrm{w}} - T_{\mathrm{p,i}}\right)\rho_{\mathrm{p}}\, c_{\mathrm{P,p}}\, C_{\mu,\mathrm{p}}^{1/4} k_{\mathrm{p,i}}^{1/2}}{A_{\mathrm{p}}} \tag{A2}$$

A_{p} from Eq. A2 is a parameter that depends on the local hydrodynamics. Its expression is defined along the relative position of the centroid of the cell next to the wall, with respect to the dimensionless thermal sub-layer. The dimensionless thermal length y^* is defined as (Eq. A3).

$$y* = \frac{\rho_{\mathrm{p}}\, C_{\mu,\mathrm{p}}^{1/4}\, k_{\mathrm{p,i}}^{1/2}}{\mu_{\mathrm{p}}} y_{\mathrm{i}} \tag{A3}$$

The dimensionless laminar thermal sub-layer is defined by its thickness y_{T}, which satisfies the relation (Eq. A4).

$$Pr_{\mathrm{t,p}}\left(\frac{1}{\kappa}\ln(Ey_{\mathrm{T}}) + P\right) = Pr_{\mathrm{p}} y_{\mathrm{T}} \tag{A4}$$

In Eq. A4, the turbulent Prandtl number is set to 0.85, κ is the Von Karman constant (equal to 0.4187), E is an empirical constant (equal to 9.793), Pr_{p} is the Prandtl number of phase p (Eq. A5), and P is a parameter given by Eq. A6.

$$Pr_{\mathrm{p}} = \frac{\mu_{\mathrm{p}}\, c_{\mathrm{P,p}}}{\lambda_{\mathrm{p}}} \tag{A5}$$

$$P = 9.24\left(\left(\frac{Pr_{\mathrm{p}}}{Pr_{\mathrm{t,p}}}\right)^{3/4} - 1\right)\left(1 + 0.28\,\mathrm{e}^{-0.007\,Pr_{\mathrm{p}}/Pr_{\mathrm{t,p}}}\right) \tag{A6}$$

From the results of Eqs. A3 and A4, comparison is made between y^* and y_{T}. If $y^* < y_{\mathrm{T}}$, then the cell centroid is considered to be within the thermal sub-layer, and A_{p} is defined by Eq. A7. If $y^* > y_{\mathrm{T}}$, then the cell centroid is assumed to be out of the thermal sub-layer, and A_{p} is defined by Eq. A8.

$$A_{\mathrm{p}} = Pr_{\mathrm{p}} y* \tag{A7}$$

$$A_{\mathrm{p}} = Pr_{\mathrm{t,p}}\left(\frac{1}{\kappa}\ln(Ey_{\mathrm{T}}) + P\right) \tag{A8}$$

Manuscript received Sept. 14, 2009, and revision received Nov. 12, 2009.